doi:10.1016/j.ijrobp.2009.10.064

PHYSICS CONTRIBUTIONS

INTEGRATION OF FUNCTIONAL MRI AND WHITE MATTER TRACTOGRAPHY IN STEREOTACTIC RADIOSURGERY CLINICAL PRACTICE

EVAGGELOS PANTELIS, PH.D.,*† NIKOLAOS PAPADAKIS, PH.D.,* KOSMAS VERIGOS, M.D.,*
IRENE STATHOCHRISTOPOULOU, M.D.,* CHRISTOS ANTYPAS, M.SC.,*‡ LEONIDAS LEKAS, M.D.,*
ARGYRIOS TZOURAS, M.D.,* EVANGELOS GEORGIOU, M.D.,† AND NIKOLAOS SALVARAS, M.D.*

*CyberKnife Center, Iatropolis–Magnitiki Tomografia, Athens, Greece; †Medical Physics Laboratory, Medical School, University of Athens, Athens, Greece; and ‡First Department of Radiology, Aretaieion Hospital, University of Athens, Athens, Greece

Purpose: To study the efficacy of the integration of functional magnetic resonance imaging (fMRI) and diffusion tensor imaging tractography data into stereotactic radiosurgery clinical practice.

Methods and Materials: fMRI and tractography data sets were acquired and fused with corresponding anatomical MR and computed tomography images of patients with arteriovenous malformation (AVM), astrocytoma, brain metastasis, or hemangioma and referred for stereotactic radiosurgery. The acquired data sets were imported into a CyberKnife stereotactic radiosurgery system and used to delineate the target, organs at risk, and nearby functional structures and fiber tracts. Treatment plans with and without the incorporation of the functional structures and the fiber tracts into the optimization process were developed and compared.

Results: The nearby functional structures and fiber tracts could receive doses of >50% of the maximum dose if they were excluded from the planning process. In the AVM case, the doses received by the Broadmann-17 structure and the optic tract were reduced to 700 cGy from 1,400 cGy and to 1,200 cGy from 2,000 cGy, respectively, upon inclusion into the optimization process. In the metastasis case, the motor cortex received 850 cGy instead of 1,400 cGy; and in the hemangioma case, the pyramidal tracts received 780 cGy instead of 990 cGy. In the astrocytoma case, the dose to the motor cortex bordering the lesion was reduced to 1,900 cGy from 2,100 cGy, and therefore, the biologically equivalent dose in three fractions was delivered instead.

Conclusions: Functional structures and fiber tracts could receive high doses if they were not considered during treatment planning. With the aid of fMRI and tractography images, they can be delineated and spared. © 2010 Elsevier Inc.

fMRI, Tractography, Radiosurgery, Treatment planning, CyberKnife.

INTRODUCTION

Stereotactic radiosurgery (SRS) has been widely recognized as an effective treatment modality in the management of various intracranial lesions (1-4). Because of its noninvasive nature, this procedure is considered one of the most suitable modalities for treating critically located lesions that are not easily accessible through neurosurgical approaches. Despite the benefits of radiosurgery, there is a 3% risk of radiation-induced deficits when a case of arteriovenous malformation (AVM) located in the motor cortex is treated (5). This risk increases from 12% to 19% when lesions in the thalamus, basal ganglia, or brain stem are in question (3, 6, 7).

With the aid of modern magnetic resonance imaging (MRI) techniques, functional brain areas and white matter fiber pathways can be well demarcated in imaging studies (8–10). These imaging techniques have been implemented in modern neuronavigation systems and used to guide the surgical removal of critically located intracranial lesions (11, 12). The incorporation of this information for radiosurgery planning has also been proposed (13–15). More specifically, blood oxygenation level-dependent (BOLD) functional MRI (fMRI) and diffusion tensor imaging (DTI) tractography have been used to identify functional structures and white-matter pathways of the brain, respectively, as critical volumes (i.e., volumes to which dose constraint are assigned) in treatment planning optimization strategies (14, 15). Despite the limited number of published studies that utilize these imaging techniques, it has been shown that these techniques could be useful for sparing healthy and sensitive parts of the brain from high doses of radiation (13–15). Further investigation is necessary to fully establish the efficacy of the proposed procedure.

In the present work, a procedure for acquiring fMRI activation maps and DTI tractography images using the scanner's clinically available software and incorporating them into the treatment planning process of an SRS system (Cyber-Knife robotic radiosurgery system; Accuray Inc., Sunnyvale, CA) (16) is described. The procedure was then applied to patients to be treated with SRS. The functional areas and fiber tracts in the fMRI and tractography images of each patient were delineated, to be used as additional critical volumes during treatment planning optimization. Treatment plans were developed with and without inclusion of the extra critical volumes in the optimization process and then compared to assess the usefulness of the method.

METHODS AND MATERIALS

Patient demographics

Four patients were included in the study. The first patient, a 25-year-old woman, was suffering from an AVM located adjacent to the posterior part of the visual pathway and near the calcarine sulcus at the right occipital lobe. The AVM had been partially obliterated by embolization, but 1 year later, the patient presented with a new hemorrhage and was referred to our facility for SRS. Pre-SRS clinical symptoms included partial visual field defects due to the hemorrhage. The second patient, a 34-year-old woman, had presented with focal epileptic seizures of the left hand attributed to a grade II astrocytoma located adjacent to the motor cortex at the right parietal lobe. Following a partial resection, she was referred for SRS. Pre-SRS clinical symptoms included hemiparesis of the left hand due to the surgery, which gradually improved. The third patient, a 55-year-old man, was referred for SRS of a brain metastasis located near the motor cortex at the left parietal lobe. He was originally diagnosed with non-small-cell lung cancer and had received radiation therapy for the metastasis. He was referred for SRS upon continued growth of his metastasis. The last patient was a 46-year-old man suffering from a hemorrhagic cavernous hemangioma located at the cerebral pont.

Dataset acquisition and image registration

For each patient, four different imaging studies were acquired: a computed tomography (CT) scan for radiosurgery treatment planning and for target tracking during treatment delivery; an anatomical MRI to provide a complete set of morphological MR data; a BOLD fMRI to provide brain activation maps; and a DTI to provide white matter tractography data. Axial CT images (27.1-cm field of view, 1-mm slice thickness, 0.53-mm in-plane resolution) of each patient were acquired using a 128-multislice SOMATOM definition CT scanner (Siemens AG, Erlangen, Germany). MRI volumes were acquired using a 3 T MAGNETOM Trio scanner (Siemens) with a 96 × 18 Tim engine, GRAPPA parallel imaging (17), and software for fMRI and DTI tractography data analyses. The anatomical MRI was acquired after patients received an injection of gadolinium-diethylenetriamine penta-acetic acid (Gd-DTPA), using an radiofrequency-spoiled fast low-angle SHot (FLASH) sequence (TR = 18 ms, TE = 4.88 ms, 1-mm isotropic voxel, GRAPPA factor = 2).

fMRI data were acquired using fat-saturated single-shot gradient echo planar imaging (EPI) (TR = 2,000 ms, TE = 30 ms, 3-mm isotropic voxel, no parallel imaging), which compensated for gross three-dimensional (3D) head movement in real time (18). A block design paradigm (five cycles, each with 30 sec on and 30 sec off) was employed, and stimuli were created and delivered to the patient using E-prime software version 1.2 (Psychology Software Tools Inc, Pittsburgh, PA) and fMRI hardware of NordicNeurolab (Bergen, Norway). Somatosensory (finger/toe tapping with audio cue) and visual (5-Hz flashing checkerboard) tasks were used to selectively probe functional areas relevant to each treatment region. fMRI data analysis was performed on-line by the scanner based on the principles of statistical parametric mapping (19). Brain activation was reported at a Z-score threshold of 4.

DTI was performed using fat-saturated single-shot spin-echo EPI with Stejskal-Tanner diffusion sensitization (TR = 6,300 ms, TE = 87 ms, GRAPPA factor = 2, number of averages = 4), acquiring 50 contiguous 3-mm thick axial slices with 1.7-mm in-plane resolution. The DTI acquisition scheme consisted of 1 baseline signal (b = 0) and 18 diffusion-weighted signals acquired along an equal number of isotropic gradient directions at the same b value of 1,000 sec/mm^2. DTI data analysis was performed on-line by the scanner, based on the assumption of Gaussian diffusion for each voxel. A color-coded fractional anisotropy (FA) map and a tensor dataset that contained information about the DT eigenvalues and eigenvectors for every voxel were produced.

The fMRI raw images were fused with the anatomical MRI data for each patient. The registration parameters were then applied to the fMRI activation maps so that the latter were registered with the anatomical MRI images. Similarly, the color-coded FA maps were fused with the anatomical MRI images. Regions of interest were drawn on the fused FA maps, and tractography calculations were performed based on the direction of the principal eigenvector of the DT (20). Calculations employed a fourth-order Runge-Kutta method, an FA threshold value of 0.2, a tract angular change of 30°, and a maximum number of tracts per voxel of 4. Figure 1 shows the AVM patient's CT, anatomical MRI, fMRI activation map overlaid on the anatomical MRI, and the FA map used for tractography calculations.

The fused fMRI activation maps and the white matter tracts overlaid on the anatomical MRI volume were exported as separate gray-scale dicom images to the CyberKnife system and loaded onto MultiPlan treatment planning system (TPS) software version 3.1. The anatomical MRI images were registered with the CT volume for each patient, using the registration algorithm of the TPS. The registration parameters were then applied to the imported fMRI activation maps and on the tractography data sets in order to attain the fusion of the activation maps and the tractography images with the CT study. Figure 2 shows the fused activation maps and tractography images overlaid on the corresponding axial, coronal, and sagittal CT planes for the AVM case.

Volume of interest delineation

The target and organs at risk (OARs), i.e., brain stem, optic chiasm, and optic nerves, were delineated using CT/anatomical MRI images. Both eyes were also contoured to avoid beam direction passing through them during treatment planning. The functional structures of the brain and the fiber tracts situated near the target were delineated by a neurosurgeon, using the fused activation maps and tractography images. In the AVM case, the Broadmann-17 structure and the ipsilateral posterior part of the optic pathway in the right occipital lobe were delineated and found to lie within 5 mm and 2.5 mm of the AVM, respectively. No effort was made to delineate the contralateral functional structures and optic pathway because they lay at a relatively safe distance from the target. Similarly, for the patients with the astrocytoma and the brain metastasis, the nearby motor cortex and pyramidal tract were contoured. The motor cortex was abutting the astrocytoma lesion and was found to lie within 2 mm of the target, in the brain metastasis case. The
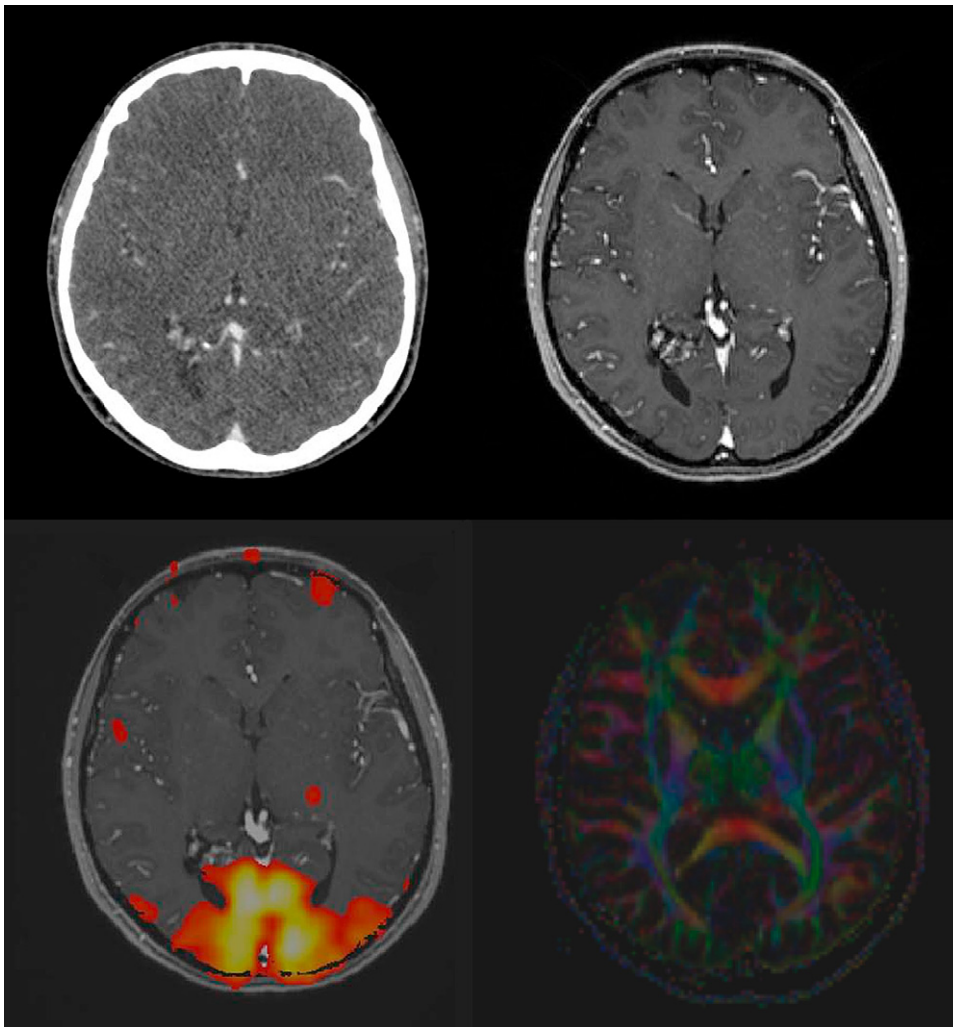
Fig. 1. (Top row) Acquired axial CT and anatomical MRI slices from the AVM patient. (Bottom row left) fMRI activation map fused with the anatomical MRI data showing the Broadmann-17 functional structure and (lower right) corresponding color-coded (red = left-right; green= anterior-posterior; blue = superior-inferior). The FA map was used for calculating the tractography data.

minimum distance between the pyramidal pathway and the target was found to be 3 mm and 2.7 mm in the astrocytoma and brain metastasis cases, respectively. For the fourth case, pyramidal fiber tracts passing through the brain stem were identified at 3.8 mm from the hemangioma.

Treatment planning

For each case, two treatment plans were developed that used the sequential optimization tool of the TPS (21). In the first treatment plan, the target and standard morphological OARs were considered in the optimization process. In terms of the optimization tool, the maximum allowed dose values were assigned to the target and the standard OARs along with a strict order of clinical goals that were optimized according to their priority (21). Target coverage was optimized first, followed by the maximum and average allowed doses to be delivered to the standard OARs. In the second treatment plan, the functional structures and fiber tracts were included in the optimization process and treated in the same way as the standard OARs. The clinical goals for the functional structures and fiber tracts were optimized following those for the standard OARs. Tuning

structures were also employed in both treatment plans to increase conformity and the spatial dose gradient of the dose distributions.

The number and size of the collimators, as well as the maximum number of monitor units (MUs) of each beam were determined prior to each treatment plan, based on the size of the target, the distance from the critical volumes, and the desired spatial gradient of the developed distribution. According to the followed optimization strategy, the highest priority was given to target coverage in order to ensure maximum therapeutic benefit while keeping doses to standard OARs, functional structures, and fiber tracts to a minimum.

The same dose was prescribed in both treatment plans for reasons of comparability. The two treatment plans for each case were compared qualitatively in terms of isodose distribution and quantitatively with the aid of dose volume histograms (DVH) (for the target and the nearby OARs, functional structures, and fiber tracts), total number of beams and MUs, and other numerical indices calculated by the TPS. In detail, the conformity index (CI) (defined as the ratio of the volume of the prescription isodose surface to the target volume that is encompassed by the prescription isodose surface), the new conformity index (nCI) (defined as the prescription isodose volume multiplied by the target volume and then divided by the target
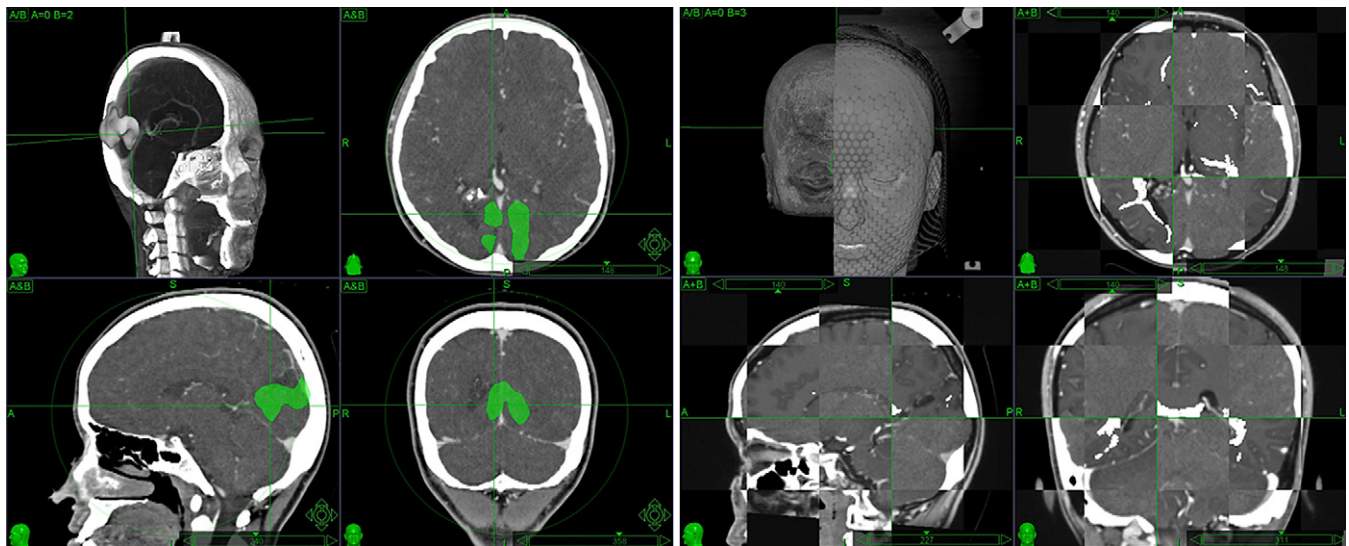
Fig. 2. Fused fMRI activation maps (left panels) and tractography data (right panels) overlaid on the CT slices in axial, sagittal, and coronal planes for the AVM case.

volume encompassed by the prescription isodose surface squared), and the homogeneity index (defined as the ratio of the maximum dose to the prescription dose) were compared.

RESULTS

In Figs. 3 to 6, the treatment plans created for the AVM, astrocytoma, brain metastasis, and brain stem hemangioma cases without and with the functional structures and fiber pathways considered in optimization process are presented in axial, sagittal, and coronal planes. In Figs. 3 and 4, the fused fMRI activation maps are overlaid on the corresponding axial, sagittal, and coronal CT planes, showing the position of the functional structures relative to the treated lesions. The delineated ipsilateral optic and pyramidal tracts are also drawn in each plane to aid in comparing the two treatment plans for each patient. Similarly, in Figs. 5 and 6, the pyramidal tract is overlaid on the axial, sagittal, and coronal CT planes of the metastatic and brain stem hemangioma cases. The delineated motor cortex situated near the metastasis is also drawn in each plane in Fig. 5. The beam configuration that corresponds to each treatment plan and the functional structures and fiber tracts of each patient are also shown in 3D space.

The results showed that functional structures and fiber tracts could receive doses (D) greater than 50% of D_{max} when not optimized for. Specifically, in the astrocytoma case, the motor cortex adjacent to the lesion received a dose of up to 2,100 cGy, which corresponds to 93% of the maximum dose. Sparing of functional structures and fiber tracts was always possible except in this case in which the motor cortex still received a maximum dose of 1,900 cGy.

Treatment plan parameters are shown in Table 1. According to the data presented, the size and/or the number of collimators had to be modified upon inclusion of the functional structures and fiber tracts in the optimization process in all cases except for the brain stem hemangioma case, where

the smallest collimator available with the CyberKnife system, the 5-mm collimator, was used in both treatment plans. In the AVM and the brain metastasis cases, the 5-mm collimator replaced the 7.5-mm collimator, and the 7.5-mm collimator replaced the 10-mm collimator, respectively, when the functional structures and fiber tracts were included in planning procedures. In the astrocytoma case, the 7.5-mm collimator was replaced by two collimators due to the relatively large volume of the lesion (2.5 cm³); a 10-mm collimator administering an isocentric configuration of beams aiming at the center of the lesion and a 5-mm collimator for a nonisocentric beam configuration to increase the spatial dose gradient.

The use of smaller collimators in the first three cases (in the astrocytoma case, only 35 of the 221 beams were delivered isocentrically, which, however, corresponds to 952 cGy of the prescribed 1,800 cGy) along with additional dose constraints for the functional structures and fiber tracts, resulted in an increase in the number of beams and MUs (Table 1) and, subsequently, in the treatment time. The correlation between extra dose constraints for nonstandard OARs and number of beams was also observed in the brain stem hemangioma case, yet the dose constraints assigned for the pyramidal tracts led to a treatment plan with more beams but less total MUs and thus similar treatment times. The conformity of the planned dose distributions was also improved (*i.e.*, the CI and nCI approached unity) when the nonstandard OARs were included in treatment planning and was attributed to the use of smaller collimators and the increase in the number of beams. The homogeneity indices of the two treatment plans with and without the nonstandard OARs are equal as the target dose was prescribed to the same isodose line in each case for ease of comparison.

Plots of target cumulative DVH data from the treatment plans for each of the four patients, DVH graphs and minimum, maximum, and average target doses, as well as target
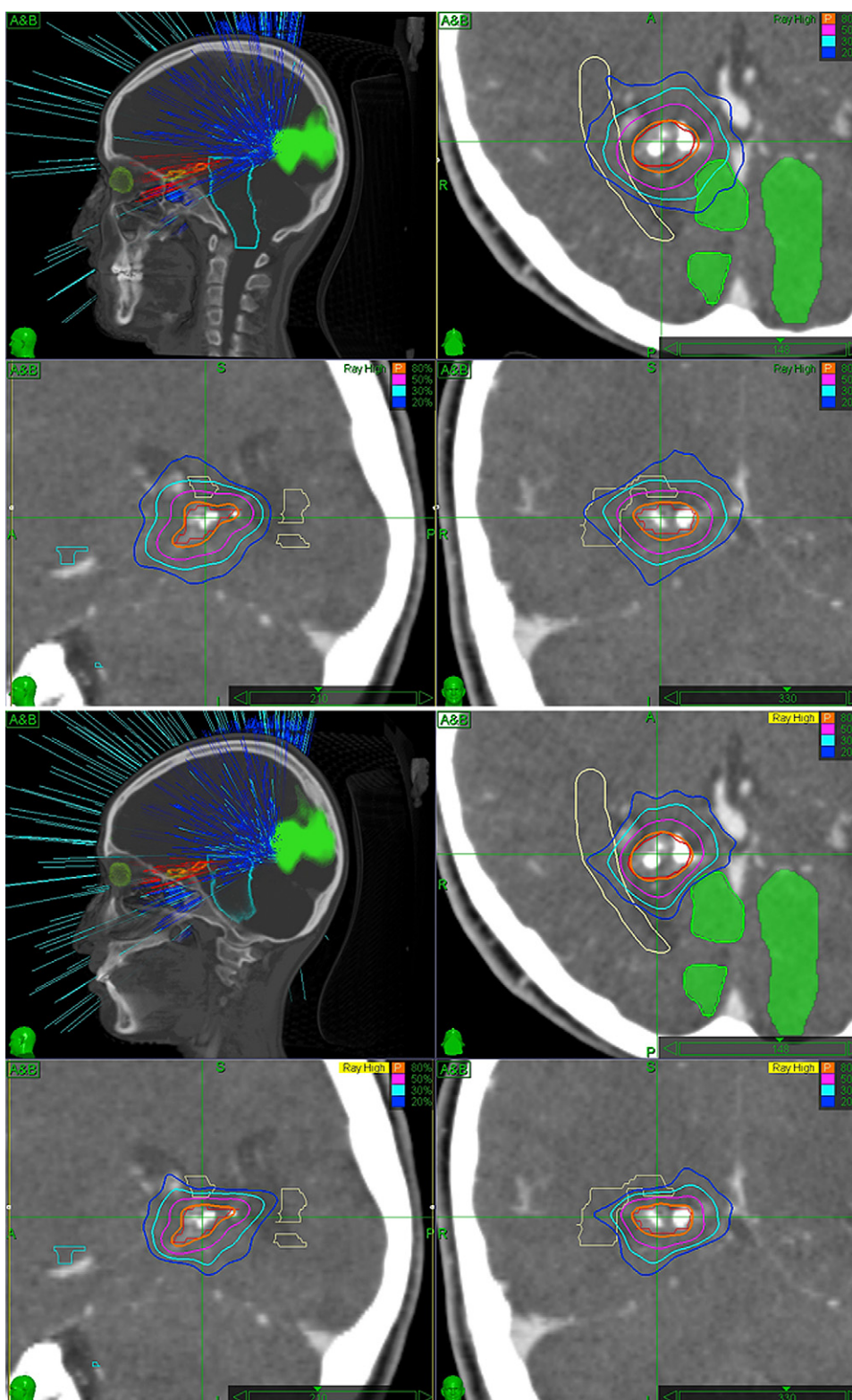
Fig. 3. Treatment plans developed without (top panels) and with (bottom panels) the introduction of the Broadmann-17 functional structure and optic tract in the optimization process for the AVM case, plotted in axial, coronal, and sagittal planes. The configuration of the beams and the Broadmann-17 structures are also depicted.

coverage in percentage points are shown in Fig. 7. Based on the data presented, the introduction of dose constraints for the functional structures and fiber tracts in treatment planning does not significantly affect the DVH values for the target.

In Fig. 8, the cumulative DVH data for the functional structures and fiber tracts in the studied cases are presented. The corresponding differential DVHs are also shown to aid the comparison between the two plans developed in each case.
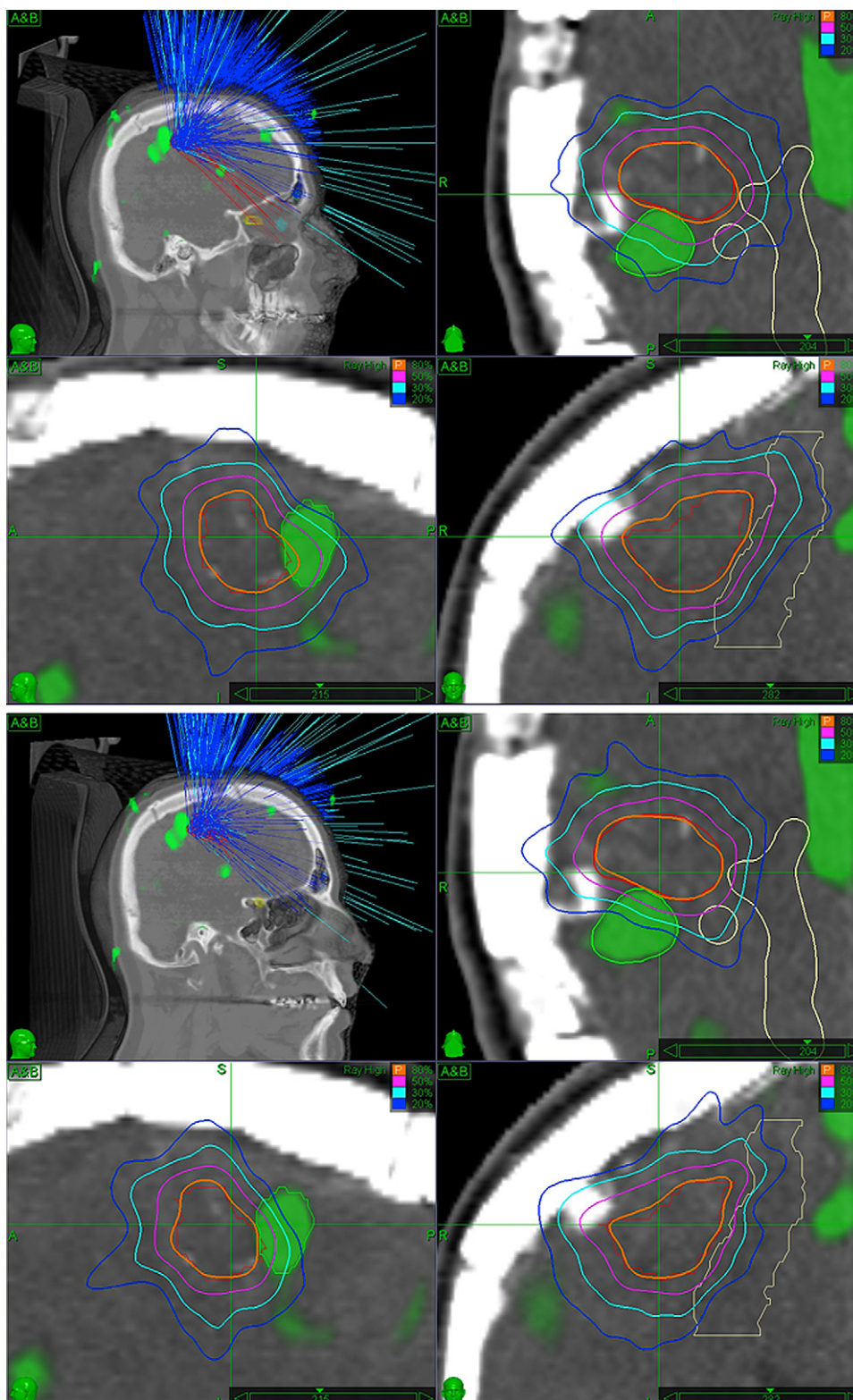
Fig. 4. Treatment plans developed without (top panels) and with (bottom panels), introducing the motor cortex and pyramidal tract in the optimization process for the astrocytoma case plotted in axial, coronal, and sagittal planes. The configurations of the beams and the motor cortex are also depicted.

DVH data shown in Fig. 8 for the functional structures and the fiber tracts before they were introduced as critical volumes confirm previous findings, as shown in Figs. 3 to 6, using the isodose distributions. In the AVM case, the

Broadmann-17 and the optic tract received doses of up to 1,400 cGy and 2,000 cGy, respectively, when ignored in treatment planning. Upon their introduction to the optimization process, a significant dose reduction was observed: the
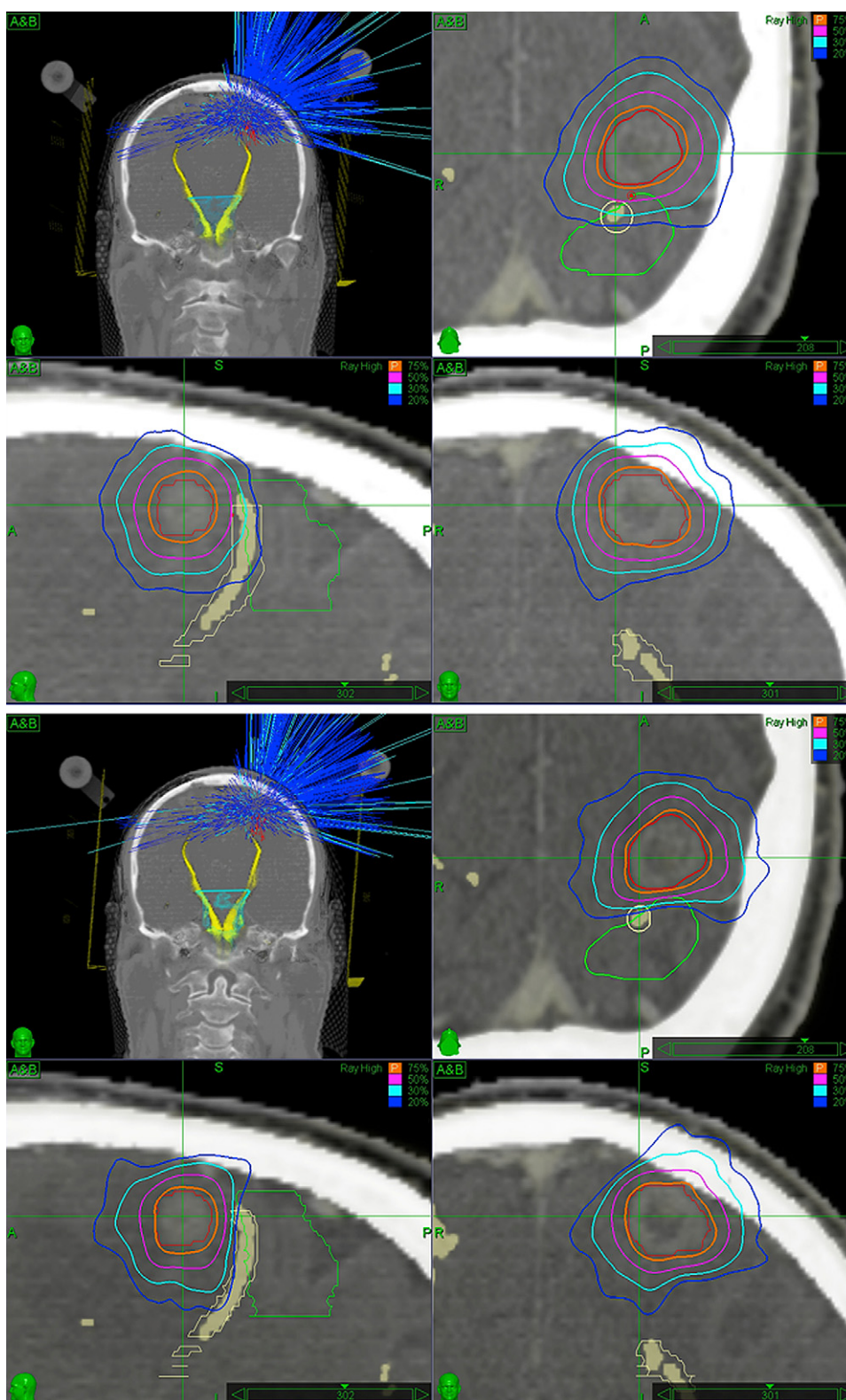
Fig. 5. Treatment plans developed without (top four panels) and with (bottom four panels), introducing the motor cortex and pyramidal tract in the optimization process for the brain metastasis case, plotted in axial, coronal, and sagittal planes. The configuration of the beams and the pyramidal tract are also depicted.

Broadmann-17 structure receiving less than 700 cGy and the optic tract less than 1,200 cGy. Moreover, the majority of the voxels comprising the OARs received less than 300 cGy. Similarly, the nearby pyramidal tracts in the brain metastasis

and brain stem hemangioma cases received less than 900 cGy instead of 1,200 cGy and less than 780 cGy instead of 990 cGy, respectively, when they were optimized for. The maximum dose to the motor cortex in the brain metastasis case
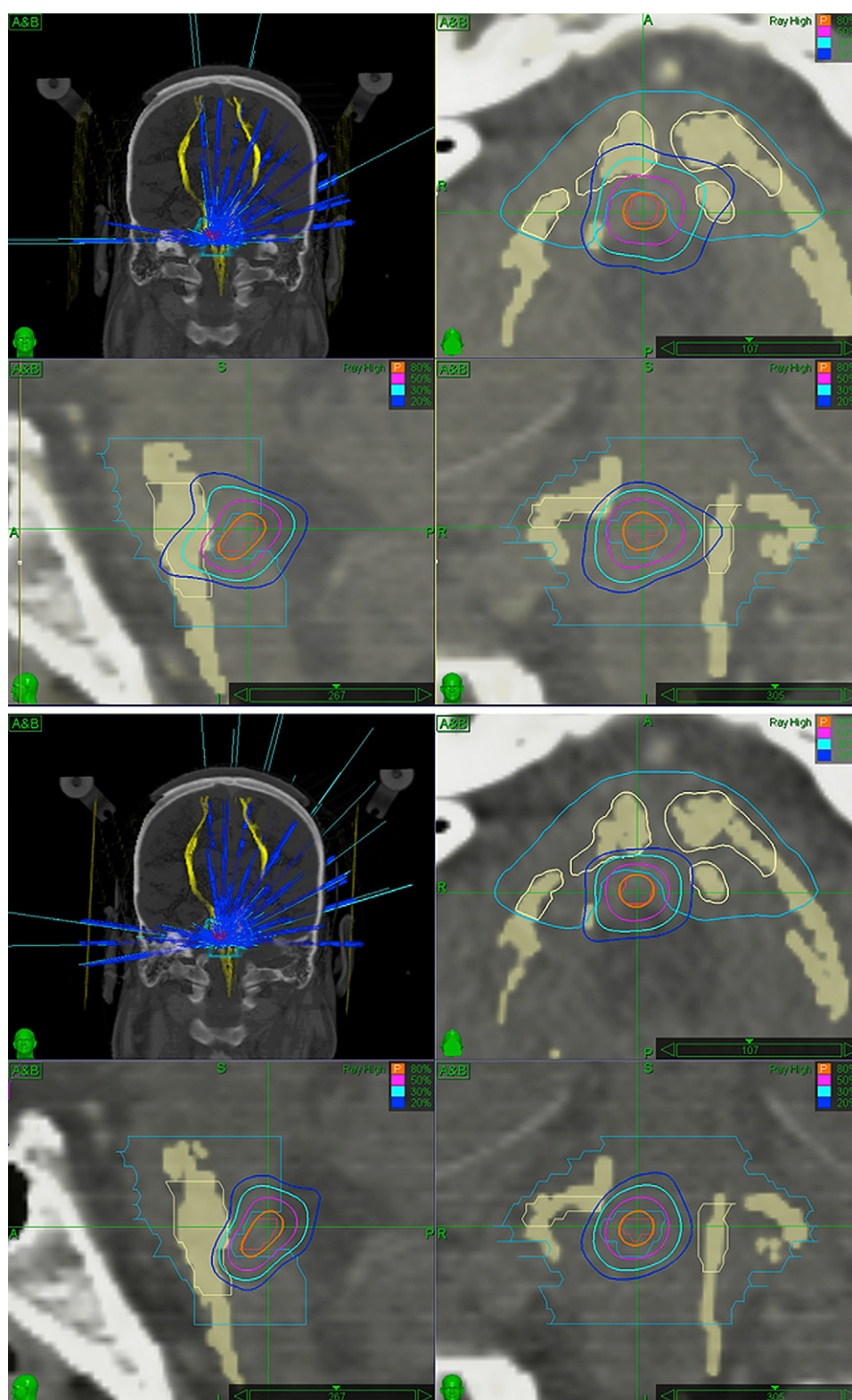
Fig. 6. Treatment plans developed without (top four panels) and with (bottom four panels) introducing the pyramidal tract in the optimization process for the brain stem hemangioma case, plotted in axial, coronal, and sagittal planes. The configuration of the beams and the pyramidal tracts are also depicted.

was reduced to 850 cGy from 1,400 cGy when included in the optimization process. Moreover, the majority of the voxels comprising this OAR received less than 150 cGy instead of 300 cGy upon inclusion. In the astrocytoma case, the av-erage dose received by the motor cortex was reduced from 800 cGy to 482 cGy and the maximum dose from 2,100 cGy to 1900 cGy when included in the optimization process. A corresponding slight change from 1,790 cGy to 1,557 cGy

Table 1. Treatment plan details with and without the inclusion of fMRI and tractography in SRS*

Case	PD(cGy)	Collimator size (mm) without/with inclusion	No. of beams without/with inclusion	MUs without/with inclusion	CI without/with inclusion	nCI without/with inclusion	HI without/with inclusion
AVM	2,300	7.5 / 5	172 / 234	18,453 / 33,331	1.37 / 1.16	1.40 / 1.23	1.25 / 1.25
Astrocytoma	1,800	7.5 / 10 and 5	139 / 221	16,389 / 22,419	1.15 / 1.09	1.23 / 1.21	1.25 / 1.25
Brain metastasis	2,300	10 / 7.5	143 / 186	13,569 / 19,203	1.31 / 1.23	1.33 / 1.23	1.33 / 1.33
Hemangioma	1,200	5	80 / 116	6,874 / 5,724	1.48 / 1.18	1.53 / 1.38	1.25 / 1.25

* Table shows prescription dose (PD), collimator size, number of beams and monitor units (MUs), conformity index (CI), new conformity indext (nCI), and homogeneity index (HI) without and with the inclusion of the nearby functional structures and fiber tracts in the optimization process for the studied cases.

was also observed in the DVH data for the pyramidal tract when they were included in the planning procedure.

DISCUSSION

Despite the submillimeter level of uncertainty in delivering the planned dose distributions in SRS (16) and the accuracy in depicting the functional areas and fiber pathways within the brain (8, 22), the procedure described above introduces an uncertainty due to the registration of different imaging volumes (*i.e.*, the fMRI and DTI data with the anatomical MRI images and the anatomical MRI with the CT images). The registration of the anatomical MRI with the CT images was found to be better than 1 imaging voxel (1 mm), using a Lucy 3D QA phantom unit (Standard Imaging Inc., Middleton, WI), allowing for accurate delineation of the target and
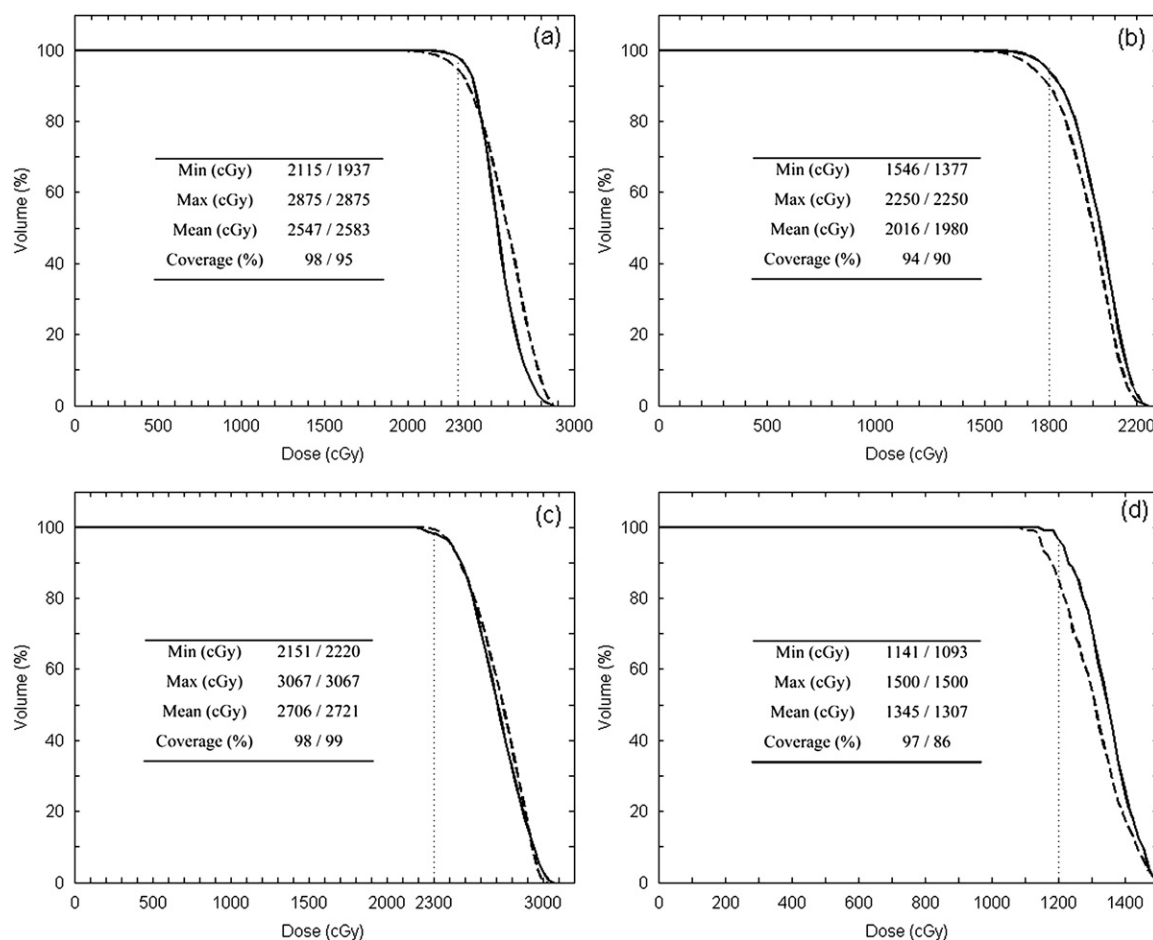

Fig. 7. Target cumulative DVH data for the AVM (a), astrocytoma (b), brain metastasis (c), and brain stem hemangioma (d) cases without (solid line) and with (dashed line) the inclusion of the functional structures and fiber tracts in the optimization process. In the inset, the corresponding minimum, maximum and average doses, as well as the target coverage in the two treatment plans (without/with, respectively) for each case are presented.
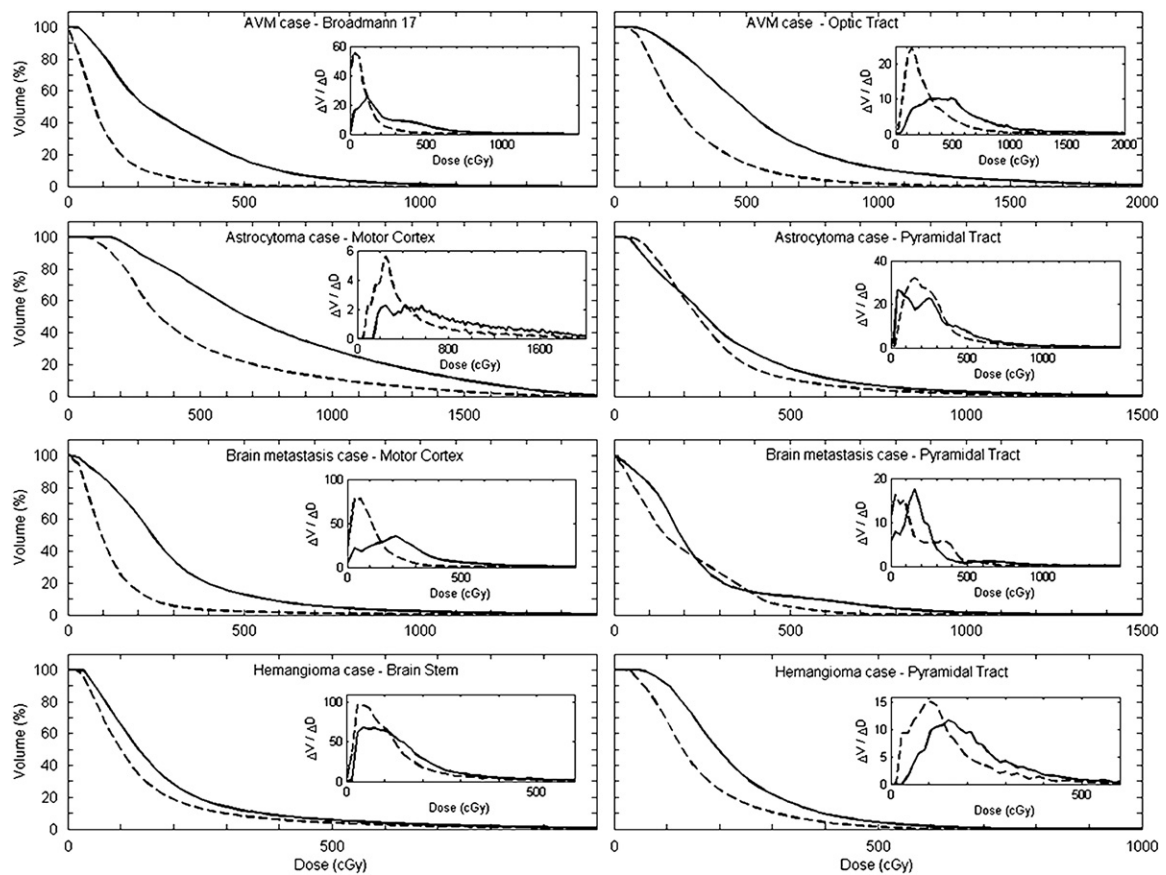
Fig. 8. Cumulative DVH data for the nearby functional structures and fiber tracts in the AVM, astrocytoma, brain metastasis, and brain stem hemangioma cases without (solid line) and with (broken line) the inclusion of the nonstandard OARs in the optimization process. In the inset, the corresponding differential DVH data are also plotted.

the OARs. Registration of fMRI and DTI data sets with anatomical MRI images is affected by nonlinear geometric distortions of EPI images used for fMRI and DTI acquisition. In this work, nonlinear automated shimming was performed prior to fMRI and DTI acquisitions for optimizing the homogeneity of the magnetic field over the imaging volume, and parallel imaging was used for acquiring the EPI data in order to minimize this effect (23). As a result, registration of the fMRI and DTI data with the corresponding anatomical MRI images suffers from an uncertainty of the order of 1 imaging voxel (3 mm), which is satisfactory for the purposes of this study (Fig. 2) and better than the accuracy that could be achieved by delineating the functional areas and fiber tracts with the aid of neurological maps. On the other hand, using the scanner's software to calculate the fMRI and tractography data sets and then fusing them with anatomical MRI volumes renders the described procedure easily available to other radiosurgery sites with access to modern MRI facilities.

Treatment plans developed with or without the inclusion of the functional structures and fiber tracts resulted in similar target coverage. This could be attributed to the fact that target coverage was given the highest priority in the hierarchy of priorities chosen during the plan optimization process. Moreover, any small differences in target coverage between the

two plans in each case actually reflect the relaxation values assigned to the dose constraints for the target.

Results showed that delineation of the functional structures and fiber tracts is beneficial and could aid users to further reduce the doses received to these healthy tissues and thus decrease the risk of radiation-induced complications and increase the quality of the delivered treatment. This is especially vital when treating AVM lesions situated in critical areas of the brain (13–15) or functional radiosurgery targets in the thalamus and basal ganglia (4) by using high doses of radiation.

In the AVM case, the optic tract that lay within 3 mm of the target received a maximum dose of 2,000 cGy when not included in the optimization process, a dose that has been linked to the development of visual field deficits (14). Upon inclusion in the optimization process, the optic tract was spared, receiving less than 1,200 cGy. Similarly, the nearby Broadmann-17 structure received less than 700 cGy when included compared to 1,400 cGy when not included. Similar results were also observed in the brain metastasis and brain stem hemangioma cases, suggesting that a few millimeters were enough for the optimization algorithm to change the beam weights and directions and spare the specific nonstandard OARs. In the astrocytoma case, on the other hand, the maximum dose experienced a modest reduction

from 2,100 cGy to 1,900 cGy when it was included in the optimization process, as the lesion was bordering the functional structure. Although this maximum dose was lower than the original scenario, it was still unacceptable, and any further effort to reduce the dose led to unacceptable target dose coverage. Therefore, the biologically equivalent dose in case of three fractions was calculated and delivered in three sessions for this patient (24).

The dose reduction for the functional structures and fiber tracts is not attributed solely to the optimization algorithm but also to the smaller collimator sizes used in the treatment plans developed with their inclusion in the optimization process. The contribution of the smaller collimator size, however, was found to be relatively small compared to the inclusion of clinical goals for the nonstandard OARs in the optimization process. For example, in the AVM case, the Broadmann-17 and optic tract received less than 1,100 cGy and 1,850 cGy, respectively, when ignored in the optimization process but using the 5-mm collimator. Although these

doses were lower than those obtained with the 7.5-mm collimator, they were still greater than the 700 cGy and 1,200 cGy calculated when the structures were included in the optimization process.

CONCLUSIONS

In conclusion, it is beneficial to incorporate BOLD fMRI activation maps and DTI tractography images into radiosurgery clinical practice. Functional structures of the brain and white matter fiber pathways could receive high doses of radiation depending on their distance from the treated lesion. With the aid of the above-described techniques, these structures can be marked as critical structures and spared during treatment planning process. In cases where this is not feasible due to close proximity of the critical volumes to the treated lesions, the biologically equivalent dose could be delivered in more than one fraction to reduce the risk for any radiation-induced complications.

REFERENCES

1. Chopra R, Kondziolka D, Niranjan A, *et al* Long-term follow-up of acoustic schwannoma radiosurgery with marginal tumor doses of 12 to 13 Gy. *Int J Radiat Oncol Biol Phys* 2007; 68(3):845–851.
2. Mehta MP, Tsao MN, Whelan TJ, *et al* The American Society for Therapeutic Radiology and Oncology (ASTRO) evidence-based review of the role of radiosurgery for brain metastases. *Int J Radiat Oncol Biol Phys* 2005;63:37–46.
3. Pollock BE, Gorman DA, Brown PD. Radiosurgery for arteriovenous malformations of the basal ganglia, thalamus, and brainstem. *J Neurosurg* 2004;100:210–214.
4. Stancanello J, Romanelli P, Pantelis E, *et al* Atlas-based functional radiosurgery: Early results. *Med Phys* 2009;36(2): 457–463.
5. Hadjipanayis CG, Levy EI, Niranjan A, *et al* Stereotactic radiosurgery for motor cortex region arteriovenous malformations. *Neurosurgery* 2001;48:70–77.
6. Sasaki T, Kurita H, Saito I, *et al* Arteriovenous malformations in the basal ganglia and thalamus: Management and results in 101 cases. *J Neurosurg* 1998;88:285–292.
7. Andrade-Souza YM, Zadeh G, Scora D, *et al* Radiosurgery for basal ganglia, internal capsule, and thalamus arteriovenous malformation: Clinical outcome. *Neurosurgery* 2005;56:56–64.
8. Kim PE, Singh M. Functional magnetic resonance imaging for brain mapping in neurosurgery. *Neurosurg Focus* 2003;15(1): 1–7.
9. Faro SH, Mohamed FB, editors. Clinical functional MRI: Presurgical functional MRI: Basic principles and clinical applications. New York: Springer; 2006.
10. Melhem ER, Mori S, Mukundan G, *et al* Diffusion tensor MR imaging of the brain and white matter tractography. *AJR Am J Roentgenol* 2002;178:3–15.
11. Kamada K, Todo T, Masutani Y, *et al* Combined use of tractography-integrated functional neuronavigation and direct fiber simulation. *J Neurosurg* 2005;102:664–672.
12. Pirotte B, Voordecker P, Neuroschl C, *et al* Combination of functional magnetic resonance imaging-guided neuronavigation and intraoperative cortical brain mapping improves target-

ing of motor cortex stimulation in neuropathic pain. *Neurosurgery* 2003;56:344–359.
13. Maruyama K, Kamada K, Ata T, *et al* Tolerance of pyramidal tract to gamma knife radiosurgery based on diffusion-tensor tractography. *Int J Radiat Oncol Biol Phys* 2008;70:1330–1335.
14. Maruyama K, Kamada K, Shin M, *et al* Optic radiation tractography integrated into simulated treatment planning for Gamma Knife surgery. *J Neurosurg* 2007;107:721–726.
15. Stancanello J, Cavedon C, Francescon P, *et al* BOLD fMRI integration into radiosurgery treatment planning of cerebral vascular malformations. *Med Phys* 2007;34:1176–1184.
16. Antypas C, Pantelis E. Performance evaluation of a CyberKnife G4 image-guided robotic stereotactic radiosurgery system. *Phys Med Biol* 2008;53:4697–4718.
17. Griswold MA, Jakob PM, Heidemann RM, *et al* Generalized autocalibrating partially parallel acquisitions (GRAPPA). *Magn Reson Med* 2002;47(6):1202–1210.
18. Thesen S, Heid O, Mueller E, *et al* Prospective acquisition correction for head motion with image-based tracking for real-time fMRI. *Magn Reson Med* 2000;44(3):457–465.
19. Frackowiak RSJ, Friston KJ, Frith CD, *et al*, editors. Human brain function. Academic Press USA; 1997.
20. Basser PJ, Pajevic S, Pierpaoli C, *et al* In vivo fiber tractography using DT-MRI data. *Magn Reson Med* 2000;44:625–632.
21. Schlaefer A, Schweikard A. Stepwise multi-criteria optimization for robotic radiosurgery. *Med Phys* 2008;35:2094–2113.
22. Berman JI, Berger MS, Chung SW, *et al* Accuracy of diffusion tensor magnetic resonance imaging tractography assessed using intraoperative subcortical stimulation mapping and magnetic source imaging. *J Neurosurg* 2007;107:488–494.
23. deZwart JA, van Gelderen P, Kellman P, *et al* Application of sensitivity-encoded echo-planar imaging for blood oxygen level-dependent functional brain imaging. *Magn Reson Med* 2002;48:1011–1020.
24. Park C, Papiez L, Zhang S, Story M, Timmerman RD. Universal survival curve and single fraction equivalent dose: Useful tools in understanding potency of ablative radiotherapy. *Int J Radiat Oncol Biol Phys* 2008;70:847–852.